Article

Combination of Molecule-Targeted Therapy and Photodynamic Therapy Using Nanoformulated Verteporfin for Effective Uveal Melanoma Treatment

Meijiao Song,[†] Lei Zhu,[†] Lumeng Zhang, Xiaoguang Ge, Jinfeng Cao, Yong Teng, and Rui Tian*

Cite This: *Mol. Pharmaceutics* 2024, 21, 2340−2350

Read Online

ACCESS | Metrics & More | Article Recommendations | SI Supporting Information

ABSTRACT: Uveal melanoma (UM) is the most common primary ocular malignancy in adults and has high mortality. Recurrence, metastasis, and therapeutic resistance are frequently observed in UM, but no beneficial systemic therapy is available, presenting an urgent need for developing effective therapeutic drugs. Verteporfin (VP) is a photosensitizer and a Yes-Associated Protein (YAP) inhibitor that has been used in clinical practice. However, VP's lack of tumor targetability, poor biocompatibility, and relatively low treatment efficacy hamper its application in UM management. Herein, we developed a biocompatible CD44-targeting hyaluronic acid nanoparticle (HANP) carrying VP (HANP/VP) to improve UM treatment efficacy. We found that HANP/VP showed a stronger inhibitory effect on cell proliferation than that of free VP in UM cells. Systemic delivery of HANP/VP led to targeted accumulation in the UM-tumor-bearing mouse model. Notably, HANP/VP mediated photodynamic therapy (PDT) significantly inhibited UM tumor growth after laser irradiation compared with no treatment or free VP treatment. Consistently, in HANP/VP treated tumors after laser irradiation, the tumor proliferation and YAP expression level were decreased, while the apoptotic tumor cell and CD8+ immune cell levels were elevated, contributing to effective tumor growth inhibition. Overall, the results of this preclinical study showed that HANP/VP is an effective nanomedicine for tumor treatment through PDT and inhibition of YAP in the UM tumor mouse model. Combining phototherapy and molecular-targeted therapy offers a promising approach for aggressive UM management.

KEYWORDS: uveal melanoma, verteporfin, drug delivery, targeted therapy, hyaluronic acid, nanoparticle
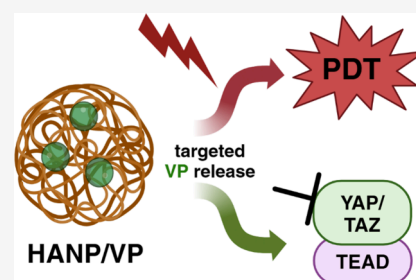
INTRODUCTION

Melanomas derived from the choroid, ciliary body, and iris of the eye are defined as uveal melanoma (UM). It is the most common primary intraocular malignancy in adults.[1,2] Although UM only accounts for 3−5% of all melanoma diagnoses, the prognosis of patients with UM is extremely poor, and nearly 50% of UM patients will develop metastatic disease with about a 13% mortality rate.[3−6] The median survival of patients with advanced UM is only 4−6 months after diagnosis.[7] Current first-line treatment options, including surgical enucleation, plaque brachytherapy, and eye removal, provide effective management of primary UM, but the overall survival of UM patients has not improved due to the high recurrence, metastasis, and therapy resistance of UM tumors.[8−10] Hence, there remains an urgent need to improve existing treatment strategies and develop effective new therapeutic approaches for the systematic treatment of primary UM and prevention of distant metastasis and recurrence.

Photodynamic therapy (PDT) is a potent therapeutic method for many cancers, including eye cancers, due to its advantages of minimal invasiveness, limited damage to vision, and low toxicity to normal tissue.[11−15] In PDT, a photosensitizer is noninvasively stimulated by light at a specific wavelength, and then, it transfers its absorbed photon energy to oxygen molecules to create reactive oxygen species (ROS), resulting in selective destruction of tumor cells and their surrounding vasculature to inhibit tumor growth.[16−18] PDT has been approved by the Food and Drug Administration (FDA) for different types of tumor treatment such as Barrett esophageal cancer, non-small-cell lung cancer, and squamous cell skin cancer.[19,20] Meaningfully, recent clinical studies have reported that 67−80% of choroidal melanoma (CM) can be completely regressed without affecting vision within 5 years in patients who received standard-fluence PDT,[21−24] suggesting that PDT could be an alternative method for eye cancer treatment that preserves patients' vision by avoiding the retinopathy associated with conventional radiation treatments.[25] However, PDT is not generally used as a primary treatment for UM in clinical practice so far, which may be attributed to the relatively low efficiency of PDT in the

prevention of aggressive UM development[26,27] despite its effective tumor control in solid tumors and CM patients.

Verteporfin (VP, trade name Visudyne), a benzoporphyrin derivative, has a long absorption wavelength that is desirable to target deep disease foci. It has been used to eliminate age-related macular degeneration, pathologic myopia, and ocular histoplasmosis syndrome as a photosensitizer for over 20 years.[28,29] At present, VP is being tested in several clinical trials for solid tumor treatment, and it has been demonstrated to be safe and effective in pancreatic and breast cancer patients.[30,31] To improve its effectiveness in cancer treatment and reduce its side effects, a series of preclinical studies have been performed to increase the targetability, specificity, and biocompatibility of VP.[32−34] For instance, VP has been conjugated with epidermal growth factor receptor (EGFR) monoclonal antibody to improve its tumor targetability, reportedly achieving a synergistic photoimmunotherapy effect in EGFR-overexpressing cells compared to VP alone without modifications.[35] Moreover, VP has been covalently modified with different mitochondria targeting moieties and reported to present improved cytotoxicity in epidermoid carcinoma (KB) cells after PDT.[36] Furthermore, VP conjugated poly(vinyl alcohol) (PVA) polymer exhibited increased efficacy in causing choroidal neovascularization (CNV) closure after PDT compared to the controls in a rat laser-injury model. With the development of nanotechnology, nanoformulated VP presented improved inhibition efficacy on tumor cell proliferation and tumor growth.[37−40] These results support the notion that VP is a potential photosensitizer for the treatment of various diseases, including UM.

In addition to mediating PDT as a photosensitizer, studies have reported that VP can also block the interaction of YAP with transcriptional enhanced associate domain (TEAD), which, in turn, blocks transcriptional activation of YAP downstream targets and inhibit tumor growth.[41−47] When dephosphorylated, YAP will bind to TEAD and mediate the expression of different oncogenes, including those that regulate the tumor cell cycle, apoptosis, epithelial mesenchymal transition, migration, invasion, and chemoresistance, indicating another role of VP in cancer management.[48,49] As a result, VP, even without light activation, alone or in combination with chemotherapy, has shown potent tumor cell growth inhibition via disruption of the YAP-TEAD complex and prevention of YAP-induced oncogenic growth in various malignancies.[50,51] Since UM cells highly express YAP genes,[41,52] VP treatment triggers the intrinsic apoptosis pathway, thus inhibiting the migration and invasion of UM cells by inhibiting the YAP-TEAD4 interaction.[42] Notably, a synergistic cytotoxic effect was observed in UM cells when VP was combined with a conventional chemotherapeutic agent.[42,53] These findings suggest that VP not only prevents UM cell proliferation but also sensitizes UM cells to chemotherapy drugs, which can potentially augment the efficacy of VP in UM treatment. Nevertheless, most current studies related to VP-mediated PDT or YAP-targeted therapy primarily focus on UM cell studies *in vitro* or require local administration *in vivo*, largely due to the inherent poor water solubility, low target selectivity, and nonspecific normal organ accumulation of VP. This hinders the clinical application of VP, so it is necessary to improve the UM treatment efficacy and reduce the systemic side effects of VP.[27]

In this study, we investigated the tumor-targeting and therapeutic effects of a biodegradable nanoformulated VP in an UM mouse model. To enhance biocompatibility and tumor-specific delivery, VP was encapsulated within biodegradable polymeric hyaluronic acid nanoparticles (HANP/VPs). Hyaluronic acid (HA) is a crucial component of the eye's extracellular matrix and has a long history of safe use in ocular disease treatment without causing ocular tissue toxicity.[16,54−59] HA can be chemically conjugated with hydrophobic components, resulting in the self-assembly of amphiphilic nanoparticles. These nanoparticles possess a hydrophilic outer layer with CD44-binding properties, along with hydrophobic cavities for encapsulating hydrophobic agents.[16,60−62] Nano-formulated VP remained stably dispersed in physiological buffers (H_2O, PBS, and DMEM) for over 7 days without visible precipitation or changes in the diameter. In contrast, HANP exhibited enzyme-responsive drug release, as 76% ± 7% of VP was released from the HANP/VP complex within 30 h when incubated with hyaluronidase, leading to effective tumor cell inhibition *in vitro*. Given that CD44, the specific ligand of HA, is strongly expressed in UM,[63] HANP/VP was expected to preferentially accumulate in UM through active receptor binding and passive enhanced permeability and retention (EPR) effects, facilitating drug delivery and enhancing tumor growth inhibition in UM. Indeed, our results showed that 24 h after intravenous injection (at an equivalent dose of 5 mg/kg of VP), HANP/VP was highly concentrated at UM mouse tumor sites (3-fold higher than that of free VP), with low uptake in normal organs, indicating effective tumor targeting and minimal tissue toxicity. Following deep red laser irradiation (690 nm, 500 mW cm^{-2}, 10 min), we observed significant tumor growth inhibition in UM tumors treated with HANP/VP compared to nontreated and free VP-treated UM tumors. Histological staining confirmed reduced tumor cell proliferation, decreased levels of YAP protein, and increased apoptosis in HANP/VP-treated UM tumors. Notably, CD68+ M1-type macrophages and CD8+ activated T cells increased in number following the HANP/VP treatment combined with deep red laser irradiation, contributing to the improved tumor-suppressing effect of the HANP/VP treatment. Overall, our findings highlight the potential of HANP/VP as a promising nanomedicine for UM treatment. To the best of our knowledge, this is the first study to harness the PDT and molecular targeting therapy capabilities of VP in UM treatment.

■ MATERIALS AND METHODS

Reagents. HA was purchased from Huaxi Biotechnology (200 kDa, Shandong, China). Verteporfin, tetrabutylammonium hydroxide (TBA), 5β-cholanic acid (CA), and propidium iodide (PI) were obtained from Sigma-Aldrich Co. (St. Louis, MO, USA). RPMI-1640 and Dulbecco's modified Eagle's medium were purchased from Gibco (Carlsbad, CA, USA). Human melanoma cell line 92−1 was purchased from Leiden University Medical Center laboratory (Leiden, The Netherlands). Mouse melanoma cell line B16F10 was purchased from ATCC (Manassas, VA). The dichlorodihydrofluorescindiacetate (DCFDA) kit was obtained from Meilunbio Co., Ltd. Cell Counting Kit-8 (CCK-8) was obtained from Beyotime Biotechnology Co., Ltd.

Synthesis and Characterization of HANP and HANP/VP vesicles. HA was mixed with the salt tetrabutylammonium (TBA) at 50 °C overnight and lyophilized. The product, HA-TBA, was then chemically modified with ethylenediamine (EDA)-modified 5β-cholanic acid (CA) in the presence of

EDC and NHS at 60 °C at a substitution rate of 10%, which contains 10 CA molecules per 100 disaccharide units in HA.[60] To load VP into HANP, 80 mg of HANP was dispersed in 15 mL of distilled water and homogenized in a high-pressure homogenizer (D3-L, PhD Technology, Saint Paul, MN) for 5 min. After that, VP in 1 mL of DMSO was added, and the mixture was homogenized for another 5 min. The resulting solution was dialyzed against distilled water for 4 h to remove the free drug and organic solvent before being freeze-dried.

Characterization of HANP/VP. HANP and HANP/VP were dispersed in ultrapure water and dropped onto the surface of a special copper mesh for electron microscopy. After air drying, the morphology of the HANP/VP was imaged by an HT7700 transmission electron microscope with a voltage of 100 kV. The diameter and zeta potential of the HANP and HANP/VP nanoparticles were determined by a Malvern Zetasizer Nano ZS (Malvern Instruments, Malvern, U.K.) at room temperature. The particle size of HANP/VP was measured over 7 days in H_2O, phosphate buffer solution (PBS, pH 7.4), and fetal bovine serum (FBS) at room temperature. UV−vis absorbance spectra of VP, HANP, and HANP/VP were measured with a Multiskan GO microplate reader (Thermo Fisher Scientific, MA, USA). Fluorescent signals of VP and HANP/VP were measured by using a fluorescence spectrophotometer (Varian Medical Systems, Palo Alto, USA). For absorbance and fluorescent spectrum measurements, VP was dissolved in DMSO and diluted with H_2O to a concentration of 0.01 mg/mL. Freshly prepared HANP/VP contained an equivalent amount of VP at 0.01 mg/mL in H_2O with 10% DMSO, while the HANP concentration was set at 0.01 mg/mL in H_2O with 10% DMSO.

Verteporfin Loading Efficiency and Loading Content Measurements. The encapsulation efficiency and actual drug loading capacity were determined by HPLC (Waters, Milford, MA). The liquid phase conditions were established as follows: the reverse-phase column was C18 column (5 μm, 4.6 × 250 mm^2) in a 10−65% linear gradient of an acetonitrile/water mixture (containing 0.1% trifluoroacetic acid) for 30 min at a flow rate of 1 mL/min. The detection wavelength was set as 435 nm with a UV detector. The VP content was quantified using the predetermined standard curve: $y = 10.01x + 0.0183$ ($R^2 = 0.9950$), derived by plotting the peak area of free VP in HPLC against gradient-diluted VP concentrations ranging from 0.08 to 0.01 mg/mL. The encapsulation efficiency (EE) and loading capacity (LC) were calculated as follows:

$$EE \% = \frac{\text{Amount of VP in micelles}}{\text{Total amount of VP added}} \times 100\%$$

$$LC \% = \frac{\text{Amount of VP in micelles}}{\text{Weight of micelles}} \times 100\%$$

In Vitro VP Release Profile of HANP/VP. The release profiles of VP from HANP/VP were determined by using a dialysis method in the presence of various concentrations of hyaluronidase. Briefly, lyophilized HANP/VP (10 mg) was dispersed in 1 mL of phosphate-buffered saline (PBS, pH 5.0, 37 °C) containing different concentrations of hyaluronidase (0 and 2000 units/mL). The dispersed HANP/VP was transferred to cellulose ester dialysis tubes (molecular weight cutoff = 10000; Spectrum) immersed in 20 mL of PBS (pH 5.0, 37 °C) and gently shaken at 37 °C in a water bath at 100 rpm. A 0.2 mL aliquot was collected, and an equal volume of fresh medium was replenished at predetermined time points. The

amount of released VP was determined by HPLC at 435 nm using the standard VP curve established earlier.

Singlet Oxygen Detection. A dichlorodihydrofluorescein diacetate (DCFH-DA) assay was used to measure ROS. It is a cell-permeable nonfluorescent agent that can be hydrolyzed intracellularly to the fluorescent DCFH carboxylate anion. B16F10 cells at a density of 1×10^4 cells/well were seeded in 96-well plates and incubated in a complete medium for 24 h at 37 °C. The next day, the medium was replaced with a fresh culture medium containing HANP/VP or VP. After 4 h of incubation at 37 °C, fresh culture medium containing 10 μM DCFHDA was added, and the cells were incubated for another 20 min. Finally, the cells were irradiated with a 690 nm laser at a power of 100 mW/cm^2 for 5 min, and the fluorescence detection of dichlorofluorescein (DCF) was performed with a fluorescence microplate reader, which represents the amount of intracellular ROS.

Cytotoxicity Assay. A standard CCK-8 assay was used to measure the cell activity. The cell culture environment was 5% CO_2 at 37 °C. When 92−1 cells and B16F10 cells were confluent, they were passaged in 96-well cell culture plates and incubated with different concentrations of VP in free VP and HANP/VP, which were equivalent to VP doses of 0.4, 0.8, 1.2, 1.6, and 2.0 μM. The cells were cultured for 12 h and were irradiated with a 690 nm laser at 100 mW cm^{-2} for 5 min. Finally, the cells were cultured with 200 μL of CCK-8 (10%) and incubated for 2 h. A microplate reader was used to record the absorption of CCK-8 at 450 nm, and the relative cell viability was calculated.

***In Vivo* Fluorescence Imaging of HANP/VP in Tumors.** All animal experiments were approved by the Institutional Animal Care and Use Committee of Jilin University. Female C57BL/6 mice (4 to 5 weeks old, 18−20 g) were purchased from Shanghai SLAC Laboratory Animal Co., Ltd. The mice were maintained in a pathogen-free environment with free access to food and water. B16F10 cells (100 μL, 1×10^5 cells/mouse) were subcutaneously injected into mice thighs on both sides and the following formula was used to calculate the volume of the tumors: Width^2 × length/2. When the tumor volume reached ∼80 mm^3, the C57BL/6 mice were administered VP or HANP/VP at a 5 mg/kg dose of VP through the tail vein. *In vivo* fluorescence imaging was performed 24 h after injection with a fluorescent filter (ex/em: 488/690 nm). Then, the mice were sacrificed. Tumors and other major organs, including the heart, liver, spleen, lungs, and kidneys, were collected and imaged *ex vivo* using an IVIS system.

***In Vivo* Tumor Treatment.** The B16F10 cells (100 μL, 1×10^5) were injected subcutaneously into the thighs of mice on both sides. When the tumor sizes grew to about 80 mm^3, the tumor-bearing C57BL/6 mice were randomly divided into three groups (five mice per group): the nontreated, VP, and HANP/VP groups. These mice were administered a 5 mg/kg equivalent dose of VP. The tumors on the right side for all groups received 690 nm deep red laser irradiation at 500 mW/cm^2 for 10 min, while the tumor on the left side was shielded without laser irradiation. The mouse body weight and tumor volume were measured every 5 days. Twenty days after the treatment, tumor-bearing mice were euthanized, and tumors and normal organs were collected for histological analysis using hematoxylin and eosin (H&E) staining.

Immunostaining. The tumors were dissected and embedded in an optimal cutting temperature (OCT)

Scheme 1. Production of HANP/VP
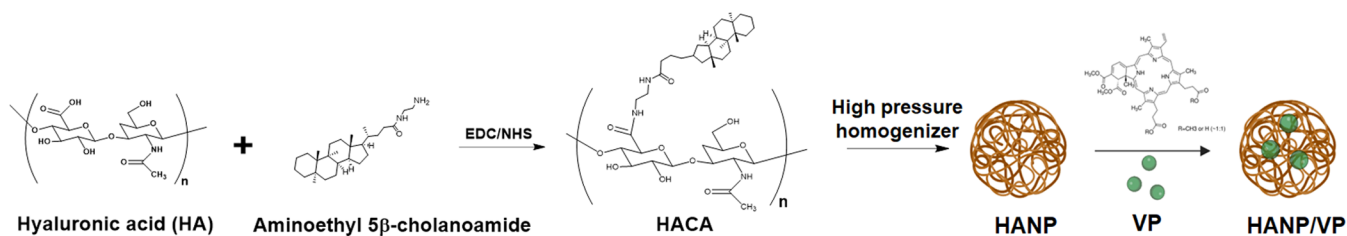
compound. These tissue blocks were sliced into 10 μm sections for immunofluorescent staining. YAP expression after treatment was detected using mouse monoclonal YAP antibody and visualized using a horseradish peroxidase (HRP) conjugated secondary antibody. To observe proliferating cells and PDT-induced apoptosis at the tumor site, Ki67 and Caspase-3 antibodies (eBioscience) were applied to stain the tumor tissues from the different treatment groups. A rat anti-mouse CD68 antibody (Bio-Rad) was used to identify M1 macrophages. Secondary antibodies against corresponding species of primary antibodies labeled with FITC, Alexa Fluor 488 dye, or Alexa Fluor 555 dye (Thermo Fisher Scientific) were used to detect biomarker-positive cells following incubation with single or dual primary antibodies. Cell nuclei were visualized with DAPI. Fluorescent images were taken by using an inverted fluorescence microscope (Olympus, Bethlehem, PA). Fluorescence images were analyzed and quantified by using the NIH ImageJ software.

Statistical Analysis. All experimental results were presented as the mean ± standard deviation from more than three repeat samples. Statistical analysis was performed using a two-tailed student's t test. A statistically significant difference was defined as a p-value less than or equal to 0.05.

■ RESULTS AND DISCUSSION

Preparation and Characterization of HANP/VP. HA is a naturally occurring, nontoxic glycosaminoglycan disaccharide polymer. It serves several crucial purposes in the human body including joint and tendon lubrication and cell-to-cell communication. Due to HA's safety profile and physiological effects, it has become an important substance in ophthalmology.[64] To specifically deliver VP to UM tumors, we modified the hydrophilic HA with a hydrophobic moiety, 5β-cholanic acid (5β-CA), to form a self-assembling hyaluronic acid nanoparticle (HANP). Hydrophobic VP was then loaded into the hydrophobic space inside HANP using a high-pressure homogenizer as described in Scheme 1 and our previous reports.[16,17,60,62]

To optimize the loading efficiency, different concentrations of VP were loaded into HANP (10%, 20%, and 40%, w/w; Table 1). When the VP to HANP ratio is set at 1:4 (w/w), 18% (w/w) VP can be loaded into HANP, resulting in a calculated loading efficacy of 90% according to a standard curve plotted using various concentrations of VP (Figure S1).

Table 1. Verteporfin (VP) Loading Efficiency under Different Conditions

HANP/VP (w/w)	loading content (%)	loading efficiency (%)
9:1	7	72
4:1	18	90
3:2	27	68

While increasing the VP input raises the loading content to 27%, the loading efficacy is quite low at 68%. Considering the production cost, we chose a VP/HANP ratio of 1:4 (w/w) in this study. It is worth mentioning that finely adjusting the HANP and VP ratios can possibly affect the loading efficacy for large-scale HANP/VP production. However, we did not assess this in the current proof-of-concept study. In our study, we utilize a high-pressure homogenizer to convert HACA into HANP before loading VP. It may be worthwhile to explore the simultaneous encapsulation of VP into HACA to form HANP/VP in future translational studies, potentially saving time and effort while achieving high loading efficiency. To confirm successful VP encapsulation, the absorbance spectra of VP and HANP/VP were measured using ultraviolet−visible−near-infrared (UV−vis−NIR) spectra. A broad absorption spectrum has been observed, but only the deep red peak at 689 nm is utilized in clinical practice, which allows good tissue penetration for PDT applications.

As shown in Figure 1a, the characterized peaks of VP at 345, 435, and 682 nm were all detected in HANP/VP. Interestingly, VP is originally fluorescent (ex/em: 488/690 nm) and can be used to track the behaviors in vitro and in vivo by fluorescent imaging. A slight quenching effect was noticed when VP was encapsulated in HANP, compared to the free VP at the same concentration (Figure 1b). The diameter of HANP was measured as around 180 nm but increased to about 200 nm after VP was loaded into HANP according to dynamic light scattering (DLS) measurement and transmission electron microscopy (TEM), as shown in Figure 1c. A nanocomplex must be stable under physiological conditions to ensure that it can be used for an in vivo study. Accordingly, we evaluated the HANP/VP stability. The zeta potential of HANP was −28 ± 5 mV, whereas that of HANP/VP was −30 ± 8 mV, indicating good stability against coalescence[65] (Figure 1d). During the 7 days of incubating HANP/VP in H$_2$O, PBS, and DMEM containing 10% FBS, the diameter of HANP/VP was not found to change significantly. We did not observe precipitations of HANP/VP in physiological buffers during this study (Figure 1e,f). Collectively, these data verified the successful construction of HANP/VP, which improved the biocompatibility and biostability of VP for further in vivo applications.

Drug Release Profile of HANP/VP. After interacting with the CD44 receptor that is overexpressed by 6- to 7-fold on tumor cells,[66,67] HA can be internalized into endosomes and degraded into oligomeric HA (oligo-HA) by hyaluronidase I (Hyal 1) under acidic conditions in the endosomes/lysosomes.[68,69] Because extracellular hyaluronidase II mainly degrades the high molecular weight (MW) HA at MW over 500 kDa, the HANP derived from 200 kDa of HA used in our study was stable in blood circulation. Thus, the CD44 targeted internalization into tumor cells ensures the release of VP in tumor cells but not in blood circulation and normal organs,
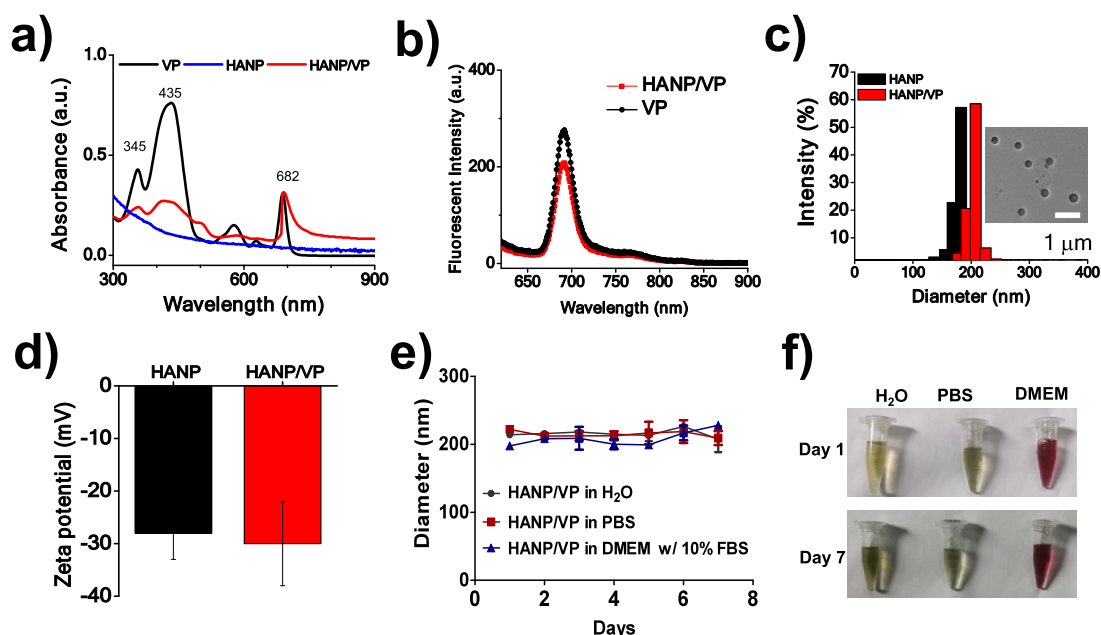
Figure 1. Characterization of HANP/VP. a) UV−vis−NIR spectrum of VP, HANP, and HANP/VP. The characterized absorbances at 345, 435, and 682 nm of VP were detected in the HANP/VP complex. HANP alone did not show an obvious absorbance at this range. b) Fluorescent spectrum of VP and HANP/VP. Both VP and HANP/VP at the same concentration (0.01 $\mu g/\mu L$) showed the fluorescent signal at 690 nm, while HANP/VP showed slightly weaker signals due to the quenching effect after encapsulation. c) The diameters of HANP and HANP/VP were determined by DLS. HANP diameter enlarged from 180 ± 52 nm to 200 ± 36 nm after VP encapsulation. Insert is a TEM image of HANP/VP. The scale bar equals 1 μm. d) Zeta potentials of HANP and HANP/VP were measured as −28 ± 5 mV and −30 ± 8 mV, respectively. e,f) Stability of HANP/VP in different buffers, including H$_2$O, PBS, and DMEM containing 10% FBS. Diameters of HANP/VP were not changed significantly during 1 week of incubation at room temperature without precipitation.

thus reducing systemic side effects *in vivo*. In Figure 2, we determined the cumulative release of VP from the HANP/VP
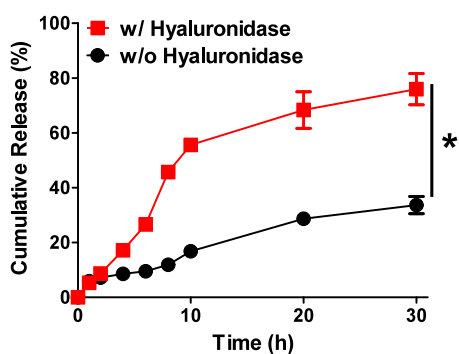

Figure 2. Cumulative VP release profile from HANP/VP as determined by HPLC. VP was found to release in a time-dependent manner from HANP/VP. The VP release was faster in the existing of Hyaluronidase. At 10 h post incubation, 55% ± 5% VP was released with Hyaluronidase, which is higher than that without hyaluronidase at 16% ± 2%. After 30 h of incubation, 76% ± 7% of VP was released with hyaluronidase, while only 31% of VP was released in the absence of Hyaluronidase. *, $p < 0.05$.

complex under acidic conditions (pH 5.0) according to the standard curve, which was established using high-performance liquid chromatography (HPLC, Figure S1).

The cumulative release of VP from HANP/VP was calculated as 55% ± 5% (w/w) in the presence of native hyaluronidase, but only 16% ± 2% (w/w) of VP was detected due to the extravasation effect without hyaluronidase in the first 10 h of incubation. At 30 h of incubation, we found that

76% ± 7% of VP was released from HANP/VP in the presence of hyaluronidase, which was about 2.2-fold higher than that of VP in the absence of hyaluronidase, suggesting that the release of VP from HANP/VP is hyaluronidase dependent.

ROS Generation of HANP/VP *In Vitro*. The generation of sufficient amounts of ROS in PDT is a key factor in effective PDT treatment. To explore the ROS-producing ability of HANP/VP after deep red laser irradiation, VP and HANP/VP incubated cells were exposed to a 690 nm laser at 100 mW/cm^2 for 5 min, and ROS generation was determined using dichlorodihydrofluorescindiacetate (DCFHDA) for detecting intracellular ROS. As shown in Figure 3a, in both HANP/VP and VP treated cells, the amount of ROS was elevated under deep red laser irradiation (690 nm laser, 100 mW/cm^2, 5 min) when the VP concentration was increased. A high amount of ROS was detected in HANP/VP treated cells, which indicated the high accumulation of HANP/VP complexes in the cells. In contrast, only a low amount of ROS was detected in free VP treated cells, which may be attributable to the nonselective tumor internalization of cells to VP. Next, to evaluate VP mediated inhibition of cell proliferation, the growth of HANP/VP and free VP treated cells was examined on two melanoma cell lines using a CCK-8 assay (Figure 3b,c). Both HANP/VP and VP showed dose-dependent tumor cell growth inhibition at 0.4, 0.8, 1.2, 1.6, and 2 μM equivalent doses of VP (Figure 3b,c). However, HANP/VP was more effective in the prevention of cell growth because of the higher cell uptake and ROS generation compared with free VP, as shown in Figure 3a. After 2 μM HANP/VP (equivalent amount of VP) treatment combined with laser irradiation treatment, 81% ± 3% of human UM cells and 90% ± 5% of mouse UM cells were dead, whereas 61% ± 4% of human UM cells and 68% ± 8% of
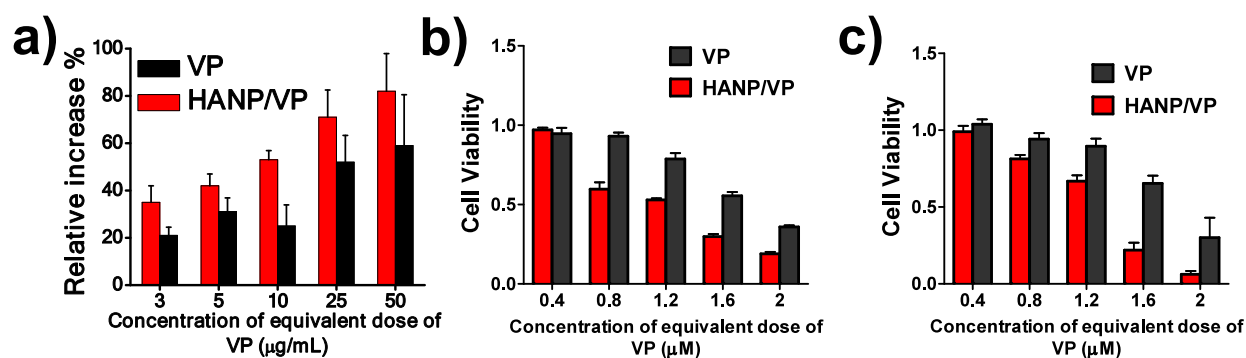
Figure 3. ROS generation and Cytotoxicity of HANP/VP. a) The quantification of HANP/VP and VP produced ROS in cells after laser irradiation (690 nm, 100 mW/cm^2, 5 min). A dose-dependent ROS amount was detected using the DCFH-DA assay. The ROS increase fold was calculated by comparing the DCF signal in treated cells and untreated cells. The inhibition of HANP/VP and VP at different concentrations to human UM cells (b, 92−1 cells) and mouse UM cells (c, B16F10 cells) after laser illumination (690 nm, 100 mW/cm^2, 5 min).
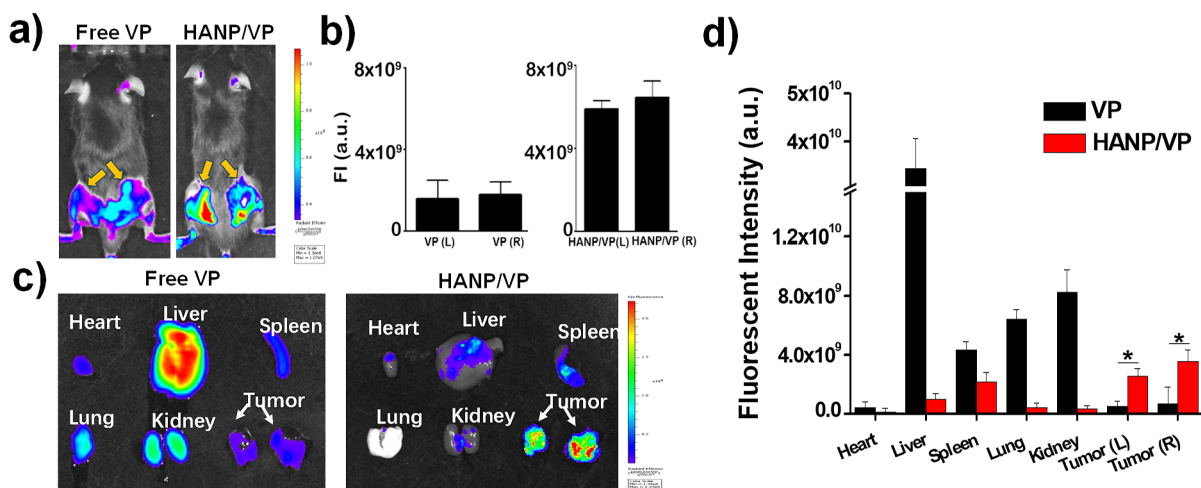

Figure 4. Fluorescent imaging of HANP/VP accumulation in the UM tumor in the mouse model. a) Whole-body imaging of a mouse bearing a B16F10 UM tumor received free VP (left) and HANP/VP (right). Arrows point to the tumor location on the thighs of both sides. b) Quantification of fluorescent signals from tumors. The HANP/VP showed remarkably strong fluorescent signals compared to free VP. c) Biodistribution and d) quantification of fluorescent signals in normal organs and UM tumors. Both tumors on each side received HANP/VP showed significantly higher signals than the tumors administrated with free VP. *, $p < 0.05$.

mouse UM cells were dead in the VP and deep red laser treated cells (Figure 3b,c). Although decreasing the VP concentration reduced the tumor cell killing effect, HANP/VP containing 0.8 μM VP still induced 42% ± 6% and 26% ± 3% of 92−1 and B16F10 cells to die, respectively. In contrast, free VP did not offer much prevention of tumor cell proliferation at concentrations lower than 1.2 μM. To assess whether the inhibition of HANP/VP and VP inhibited tumor cell proliferation in a time-dependent mannner, we chose 1 μM HANP/VP and VP to treat both 92−1 and B16F10 cells at different time points (6, 24, and 48 h) and combined with laser irradiation. We noticed that HANP/VP and VP showed stronger inhibition of tumor cells proliferation with longer incubation time, but HANP/VP is more effective than free VP (Figure S2). HANP without VP combined with deep red laser irradiation (690 nm laser, 100 mW/cm^2, 5 min) did not show obvious toxicity to either 92−1 human UM cells or B16F10 murine UM cells (Figure S3). These results illustrated that encapsulation of VP into HANP did not affect the PDT effect of VP, and the binding of HANP with CD44 on the cell surface facilitated more VP delivery into tumor cells for more effective tumor cell inhibition.

Fluorescence Imaging of Tumor Targeted Delivery of HANP/VP Following Systemic Administration. Currently, no beneficial systemic therapy is available for UM, and most UM treatment regimens are localized. Systemic therapeutic drugs are promising to eliminate invasive and distant tumor cells, thereby reducing the recurrence and metastasis of UM. Before evaluation of the treatment responses of HANP/VP in the UM model, we used whole-body fluorescent imaging to assess the tumor targeting of HANP/VP after intravenous injection. Since VP is fluorescent in the NIR range with a low tissue background, we directly injected HANP/VP into a UM model bearing a subcutaneous B16F10 tumor model. Free VP was also injected as a nontargeted control. We first evaluated the time-dependent tumor targeting of HANP/VP in B16F10 mouse model and found that a little HANP/VP was accumulated in the tumor at 6 postinjection (p.i.) and that it peaked at 24 h p.i. (Figure S4). At 48 h p.i., the majority of HANP/VP is washed out from the tumor, indicating that 24 h p.i. is optimal for HANP/VP-mediated PDT. We did not observe much free VP in the tumor, and it is washed out of the tumor within 48 h. We then examine if HANP/VP can target multiple tumors in mouse as shown in Figure 4. Consistently, strong fluorescence signals were detected from the two tumors
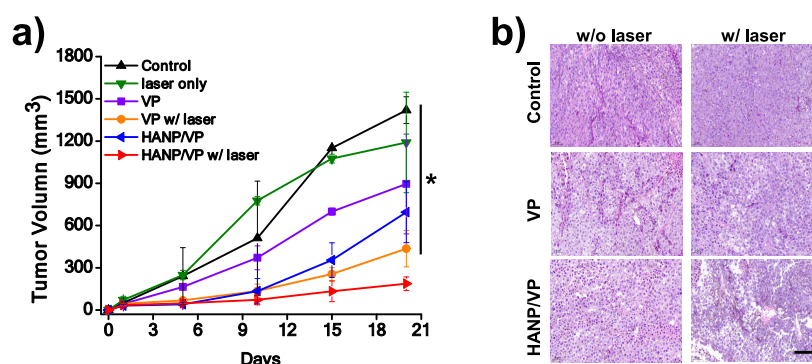
Figure 5. HANP/VP inhibited tumor growth in the UM bearing mouse model. a) Tumor growth was inhibited after HANP/VP combined with deep red laser irradiation (690 nm, 500 mW/cm^2, 10 min). Without laser irradiation, HANP/VP showed a slight prevention of tumor growth. Free VP did not significantly prevent tumor growth with or without laser irradiation. Deep red laser alone did not affect tumor growth, which is comparable to the nontreated tumors. b) H&E staining of tumors after different treatments. The tumor cells were reduced and the tumor tissue structure was disrupted after HANP/VP treatment and laser irradiation. Slight tissue damage was noticed by H&E staining in VP treated tumors. There was no detectable tissue difference between laser-irradiated tumors and nontreated tumors. Scale bar: 100 μm.
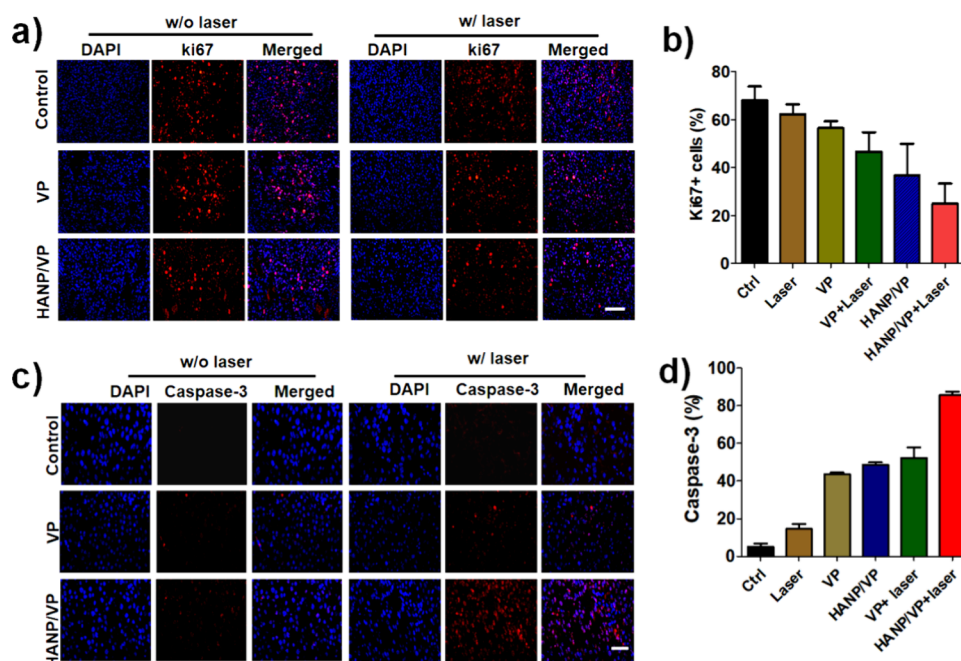

Figure 6. The tumor cells change after treatments in the tumor as stained by immunofluorescent staining. a) Proliferating cells in tumors were seen after different treatments. HANP/VP combined with laser irradiation significantly reduced the number of proliferating cells in the tumor as stained using the Ki67 antibody. b) Quantification of Ki67 positive proliferating tumor cells per image. c) Apoptotic cells were found in tumors after different treatments. HANP/VP combined with laser irradiation significantly increased the number of apoptotic cells in the tumor as stained using an active caspase-3 antibody. d) Quantification of active caspase-3 positive apoptotic cells per image.

on right and left side that received HANP/VP at 24 h p.i., whereas only weak fluorescent signals were detected from the two UM tumors treated with free VP using the fluorescent filter (ex/em: 488/690 nm). The fluorescent signal from HANP/VP treated tumors was 3-fold higher than that from VP treated tumors (Figure 4b). To further confirm the advantage of VP delivery using HANP, the tumor-bearing mice were euthanized immediately after noninvasive imaging. The major organs and tumors were collected and imaged. As shown in Figure 4c,d, a little HANP/VP was visualized in the normal organs, such as the heart, liver, lungs, kidney, and spleen, but a strong fluorescent signal from the tumor was observed due to the active CD44 targeting and passive EPR effects of HANP. On the contrary, free VP showed significantly high uptake in the liver, kidney, and lungs but low uptake in tumors, which

might be attributable to active uptake and clearance of VP from blood circulation via the high endocytic activity of liver sinusoidal endothelial cells and Kupffer cells.[70,71] Such imaging results strongly support the idea that HANP is beneficial in tumor targeted delivery and lowers the organ toxicity of VP, justifying further exploration of HANP/VP.

Synergistic Targeted therapy and PDT Efficacy of HANP/VP. Based on the improved tumor targetability and accumulation of HANP/VP, we explored the antitumor potency of HANP/VP in the subcutaneous UM model. As shown in Figure 5a, HANP/VP combined with laser irradiation significantly prevented tumor growth in 3 weeks compared to the other groups (3-fold improvement when compared to nontreated tumor, $p < 0.05$) due to the PDT effect and YAP signal pathway inhibition. Although free VP
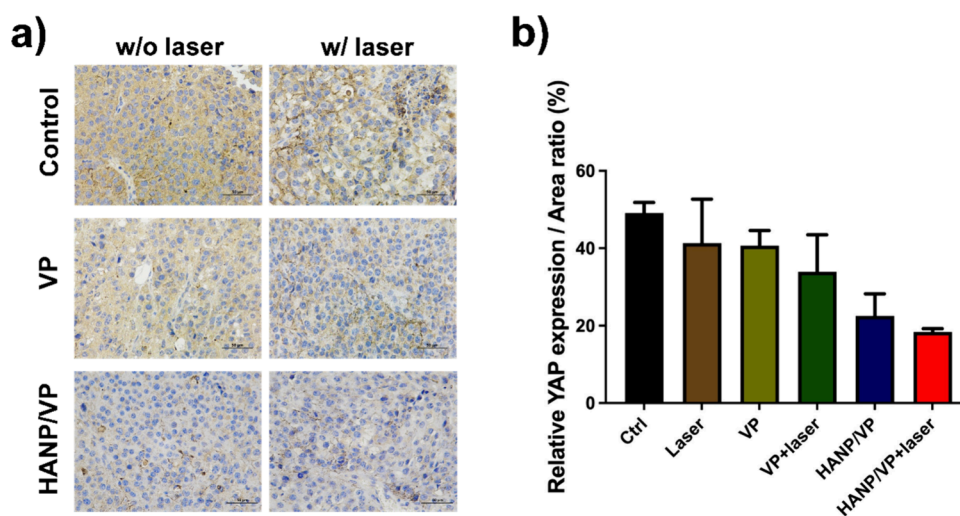
Figure 7. YAP expression changes after different treatments. a) YAP expression in the tumors was stained by immunostaining. b) Quantification of the YAP positive cells per image.

combined with laser irradiation also inhibited tumor growth, the tumor presented faster growth in the last 5 days before the control tumor reached the end point, indicating that the relatively low delivery efficiency was not sufficient to prevent tumor cell proliferation. In the absence of laser irradiation, HANP/VP treated tumors also showed about 1.8 times greater tumor growth inhibition compared to nontreated tumors. Similarly, 1.3 times greater tumor growth inhibition was noticed in the free VP without laser irradiation group, which could be caused by VP-mediated YAP signal pathway inhibition. The tumor growth rate was not significantly affected in the nontreated or laser irradiated groups. The body weight of the mice in this study did not significantly change, indicating that HANP/VP-mediated PDT did not induce systemic toxicity. To further confirm the changes in the histological features of the tumor, the normal organs and tumors from mice that received different treatments were harvested and subjected to H&E staining (Figure 5b). Histological assessment showed that HANP/VP combined with laser irradiation induced more necrosis and more severe destruction of tumor tissue compared to other groups. Only slight tumor necrosis could be observed in HANP/VP and free VP without laser irradiation groups. There was no significant tissue destruction in the nontreated and laser irradiated tumors. No obvious histological changes were observed in normal organs from all groups regardless of laser irradiation or HANP/VP treatment (Figure S5), indicating that HANP/VP selectively disrupted tumor tissue with negligible normal organ toxicity.

Furthermore, the proliferating cells were analyzed by Ki67 immunofluorescent staining (Figure 6a), revealing that HANP/VP combined with laser irradiation significantly reduced the proliferating cells ($22\% \pm 6\%$ left), while $44\% \pm 4\%$ of proliferating cells were detected in the VP combined with laser irradiation group. In the VP, laser irradiation alone, and nontreated groups, about 55−68% proliferating tumor cells were left (Figure 6b). Consistently, many apoptotic cells ($81\% \pm 7\%$) were found in the HANP/VP combined with laser irradiation group, whereas only $52\% \pm 4\%$ apoptotic cells were found in the free VP combined with laser irradiation group. Less than 45% apoptotic cells were detected in the free VP, laser irradiation alone, and nontreated groups, pointing to

low treatment efficiency in these groups due to low drug delivery efficacy.

To determine the effect of HANP/VP and VP on YAP expression after treatment, we examined the expression of YAP in tumor tissues by immunohistochemistry (IHC). Compared to the nontreated control group, the expression level of YAP was significantly downregulated in both the HANP/VP combined with laser irradiation group (by $79\% \pm 2\%$) and the HANP/VP without ser irradiation group (by $72\% \pm 5\%$) (Figure 7). The expression level of YAP was reduced by only $51\% \pm 4\%$ and $67\% \pm 6\%$ in the free VP groups with and without laser irradiation, respectively. Laser irradiation did not have much effect on YAP expression compared to that of the control group. HANP/VP provided more efficient PDT and YAP inhibition for tumor therapy.

Accumulating evidence has demonstrated that PDT induces the immunogenic death (ICD) of tumor cells, stimulates the release of tumor-related antigens in tumor cell residues, increases the infiltration of antigen-specific T cells, and reprograms tumor-associated macrophages (TAMs) into antitumor M1-like TAMs,[72,73] thereby enhancing the tumor treatment efficacy. Meanwhile, YAP has been reported to suppress T cell function and infiltration in tumors, so inhibition of YAP enhances immunotherapy responses.[74] Accordingly, we investigated whether HANP/VP mediated PDT and YAP inhibition can increase the numbers of T cells and M1-type TAMs in UM tumors to enhance the UM treatment effects. As shown in Figure 8, the number of CD8+ activated T cells in UM tumors increased after HANP/VP combined with laser irradiation ($18\% \pm 1\%$), which is much more than the nontreated ($0.4\% \pm 0.2\%$), laser irradiation ($1.16\% \pm 0.46\%$), VP ($2\% \pm 0.8\%$), VP combined with laser irradiation ($3\% \pm 0.4\%$), and HANP/VP ($8\% \pm 4\%$) treated tumors (*, $p < 0.05$). In addition, the amount of CD68+ M1-TAMs in tumors that received HANP/VP combined with laser irradiation ($9.5\% \pm 1.4\%$) were significantly higher than those in the nontreated ($1.1\% \pm 0.5\%$), laser irradiation ($1.4\% \pm 0.6\%$), VP ($3.4\% \pm 0.9\%$), VP combined with laser irradiation ($5.4\% \pm 1.5\%$), and HANP/VP ($4.9\% \pm 0.4\%$) groups (Figure 8, *, $p < 0.05$; **, $p < 0.005$). Although HANP/VP without laser irradiation also increased T cells and M1-TAMs in tumors compared to the free VP treated groups with or without laser
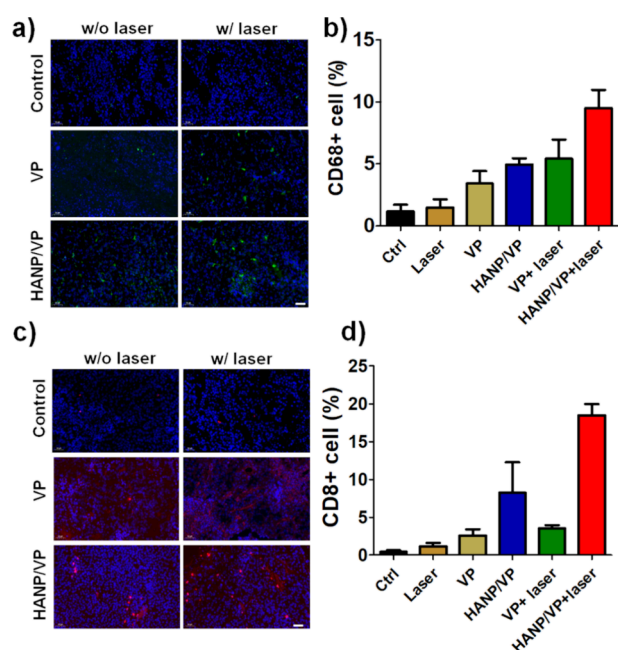
Figure 8. Immune cell changes after different treatments in tumors. a) The macrophages increased after HANP/VP combined with laser irradiation treatment as stained using the CD68 antibody. b) Quantification of CD68 positive macrophages per image. c) CD8 positive T cell changes after HANP/VP combined with laser irradiation treatment were stained using anti-CD8 antibody. d) Quantification of CD8 positive T cells per image.

irradiation due to better delivery, the HANP/VP combined with laser irradiation showed better immune response and tumor growth inhibition effect, indicating that combining PDT and YAP targeting therapy enhances tumor management.

In summary, we successfully produced a nanocomplex by encapsulation of VP into a polymeric hyaluronic acid nanoparticle (HANP/VP) for UM treatment. VP is a hydrophobic photosensitizer and YAP inhibitor and is used in this study for PDT and YAP targeted therapy. The nanoformulated VP showed improved biocompatibility and biostability with a significantly increased UM cell growth inhibition *in vitro*. After systemic delivery, HANP/VP was found to specifically accumulate in a subcutaneous UM tumor in 24 h with low organ uptake. Following one HANP/VP treatment, UM tumor growth was significantly inhibited after laser irradiation. *Ex vivo* histological analysis confirmed that more tumor cells were dead and that the majority of tissue was disrupted in tumors that received HANP/VP combined with laser irradiation. Additionally, increased amounts of M1-TAM and activated T cells were observed after HANP/VP combined with laser irradiation, implying that HANP/VP-mediated PDT and YAP inhibition achieved a synergistic tumor treatment effect. The findings of this study suggest that HANP/VP holds great promise for future clinical translation. Moreover, understanding the YAP changes and PDT effects after VP treatment will facilitate the design of novel UM treatment agents. It is worth mentioning that HANP/VP showed positive tumor immune microenvironment modulation in UM, and the combination of HANP/VP with immunotherapy agents may be valuable for metastasis and recurrent UM treatment, which is under investigation in our group.

■ ASSOCIATED CONTENT

ⓈI Supporting Information

The Supporting Information is available free of charge at https://pubs.acs.org/doi/10.1021/acs.molpharmaceut.3c01117.

> Standard curve of VP, cytotoxicity assay of HANP, cytotoxicity assay of HANP/VP on UM cells, tumor targetability of HANP/VP, and H&E staining of normal organs after different treatments (PDF)

■ AUTHOR INFORMATION

Corresponding Author

Rui Tian − *Department of Ophthalmology, The Second Hospital of Jilin University, Changchun 130000 Jilin Province, China;* ⓞ orcid.org/0000-0002-1686-1871; Email: tianrui@jlu.edu.cn

Authors

Meijiao Song − *Department of Ophthalmology, The Second Hospital of Jilin University, Changchun 130000 Jilin Province, China*

Lei Zhu − *Department of Surgery and Winship Cancer Institute, Emory University School of Medicine, Atlanta, Georgia 30322, United States*

Lumeng Zhang − *Department of Surgery and Winship Cancer Institute, Emory University School of Medicine, Atlanta, Georgia 30322, United States; Department of Nuclear Medicine, China-Japan Union Hospital, Jilin University, Changchun 130033 Jilin Province, China*

Xiaoguang Ge − *Department of Nuclear Medicine, China-Japan Union Hospital, Jilin University, Changchun 130033 Jilin Province, China*

Jinfeng Cao − *Department of Ophthalmology, The Second Hospital of Jilin University, Changchun 130000 Jilin Province, China*

Yong Teng − *Department of Hematology and Medical Oncology and Winship Cancer Institute, Emory University School of Medicine, Atlanta, Georgia 30322, United States*

Complete contact information is available at:
https://pubs.acs.org/10.1021/acs.molpharmaceut.3c01117

Author Contributions

†M. Song and L. Zhu contributed equally to this manuscript.

Notes

The authors declare no competing financial interest.

■ ACKNOWLEDGMENTS

■ REFERENCES

(1) Rantala, E. S.; Hernberg, M. M.; Piperno-Neumann, S.; et al. Metastatic Uveal Melanoma: The Final Frontier. *Prog. Retin Eye Res.* **2022**, *90*, No. 101041.

(2) Chai, P.; Jia, R.; Li, Y.; et al. Regulation of Epigenetic Homeostasis in Uveal Melanoma and Retinoblastoma. *Prog. Retin Eye Res.* 2022, 89, No. 101030.

(3) Singh, A. D.; Turell, M. E.; Topham, A. K. Uveal Melanoma: Trends in Incidence, Treatment, and Survival. *Ophthalmology* 2011, 118, 1881−1885.

(4) Nathan, P.; Hassel, J. C.; Rutkowski, P.; et al. Overall Survival Benefit with Tebentafusp in Metastatic Uveal Melanoma. *N Engl J. Med.* 2021, 385, 1196−1206.

(5) Bustamante, P.; Piquet, L.; Landreville, S.; et al. Uveal Melanoma Pathobiology: Metastasis to the Liver. *Semin Cancer Biol.* 2021, 71, 65−85.

(6) Shields, C. L.; Kaliki, S.; Shah, S. U.; et al. Iris Melanoma: Features and Prognosis in 317 Children and Adults. *J. AAPOS* 2012, 16, 10−16.

(7) Woodman, S. E. Metastatic Uveal Melanoma: Biology and Emerging Treatments. *Cancer J.* 2012, 18, 148−152.

(8) Jager, M. J.; Shields, C. L.; Cebulla, C. M.; Abdel-Rahman, M. H.; Grossniklaus, H. E.; Stern, M.-H.; Carvajal, R. D.; Belfort, R. N.; Jia, R.; Shields, J. A.; Damato, B. E. Uveal Melanoma. *Nat. Rev. Dis. Primers* 2020, 6, 24.

(9) Khoja, L.; Atenafu, E. G.; Suciu, S.; et al. Meta-Analysis in Metastatic Uveal Melanoma to Determine Progression Free and Overall Survival Benchmarks: An International Rare Cancers Initiative (Irci) Ocular Melanoma Study. *Ann. Oncol* 2019, 30, 1370−1380.

(10) Smit, K. N.; Jager, M. J.; de Klein, A.; et al. Uveal Melanoma: Towards a Molecular Understanding. *Prog. Retin Eye Res.* 2020, 75, No. 100800.

(11) Huang, J.; Zhuang, C.; Chen, J.; Chen, X.; Li, X.; Zhang, T.; Wang, B.; Feng, Q.; Zheng, X.; Gong, M.; et al. Targeted Drug/Gene/ Photodynamic Therapy Via a Stimuli-Responsive Dendritic-Polymer-Based Nanococktail for Treatment of Egfr-Tki-Resistant Non-Small-Cell Lung Cancer. *Adv. Mater.* 2022, 34, No. e2201516.

(12) Song, C.; Xu, W.; Wu, H.; Wang, X.; Gong, Q.; Liu, C.; Liu, J.; Zhou, L. Photodynamic Therapy Induces Autophagy-Mediated Cell Death in Human Colorectal Cancer Cells Via Activation of the Ros/ Jnk Signaling Pathway. *Cell Death Dis* 2020, 11, 938.

(13) Frochot, C.; Mordon, S. Update of the Situation of Clinical Photodynamic Therapy in Europe in the 2003−2018 Period. *J. Porphyrins Phthalocyanines* 2019, 23, 347−357.

(14) Zhang, W.; Zhang, X.; Shen, Y.; et al. Ultra-High Fret Efficiency Nagdf(4): Tb(3+)-Rose Bengal Biocompatible Nanocomposite for X-Ray Excited Photodynamic Therapy Application. *Biomaterials* 2018, 184, 31−40.

(15) Zhou, L.; Chen, L.; Chen, S.; Pu, Z.; Gu, M.; Shen, Y. Highly Efficient Photodynamic Therapy with Mitochondria-Targeting Aggregation-Induced Emission Photosensitizer for Retinoblastoma. *Adv. Healthc Mater.* 2023, 12, No. e2202219.

(16) Gao, S.; Wang, J.; Tian, R.; et al. Construction and Evaluation of a Targeted Hyaluronic Acid Nanoparticle/Photosensitizer Complex for Cancer Photodynamic Therapy. *ACS Appl. Mater. Interfaces* 2017, 9, 32509−32519.

(17) Xie, Q.; Gao, S.; Tian, R.; et al. Enzyme and Reactive Oxygen Species-Responsive Dual-Drug Delivery Nanocomplex for Tumor Chemo-Photodynamic Therapy. *Int. J. Nanomedicine* 2023, 18, 1−16.

(18) Gao, S.; Wang, G.; Qin, Z.; et al. Oxygen-Generating Hybrid Nanoparticles to Enhance Fluorescent/Photoacoustic/Ultrasound Imaging Guided Tumor Photodynamic Therapy. *Biomaterials* 2017, 112, 324−335.

(19) Gunaydin, G.; Gedik, M. E.; Ayan, S. Photodynamic Therapy for the Treatment and Diagnosis of Cancer-a Review of the Current Clinical Status. *Front Chem.* 2021, 9, No. 686303.

(20) Li, X.; Lovell, J. F.; Yoon, J.; et al. Clinical Development and Potential of Photothermal and Photodynamic Therapies for Cancer. *Nat. Rev. Clin Oncol* 2020, 17, 657−674.

(21) Turkoglu, E. B.; Pointdujour-Lim, R.; Mashayekhi, A.; et al. Photodynamic Therapy as Primary Treatment for Small Choroidal Melanoma. *Retina* 2019, 39, 1319−1325.

(22) Quhill, H.; Gosling, D.; Sears, K.; et al. Primary Photodynamic Therapy for Small Amelanotic Choroidal Melanomas: Consecutive Case Series of 69 Patients with at Least 24-Month Follow-Up. *Br J. Ophthalmol* 2021, 105, 794−799.

(23) Fabian, I. D.; Stacey, A. W.; Papastefanou, V.; et al. Primary Photodynamic Therapy with Verteporfin for Small Pigmented Posterior Pole Choroidal Melanoma. *Eye (Lond)* 2017, 31, 519−528.

(24) Shields, C. L.; Khoo, C. T. L.; Mazloumi, M.; et al. Photodynamic Therapy for Choroidal Metastasis Tumor Control and Visual Outcomes in 58 Cases: The 2019 Burnier International Ocular Pathology Society Lecture. *Ophthalmol Retina* 2020, 4, 310−319.

(25) Sikuade, M. J.; Salvi, S.; Rundle, P. A.; et al. Outcomes of Treatment with Stereotactic Radiosurgery or Proton Beam Therapy for Choroidal Melanoma. *Eye* 2015, 29, 1194−1198.

(26) Rundle, P. Treatment of Posterior Uveal Melanoma with Multi-Dose Photodynamic Therapy. *Br J. Ophthalmol* 2014, 98, 494−497.

(27) Rundle, P. Photodynamic Therapy for Eye Cancer. *Biomedicines* 2017, 5, 69.

(28) Blasi, M.; Pagliara, M.; Lanza, A.; Sammarco, M.; Caputo, C.; Grimaldi, G.; Scupola, A. Photodynamic Therapy in Ocular Oncology. *Biomedicines* 2018, 6, 17.

(29) Yordi, S.; Soto, H.; Bowen, R. C.; et al. Photodynamic Therapy for Choroidal Melanoma: What Is the Response Rate? *Surv Ophthalmol* 2021, 66, 552−559.

(30) Huggett, M. T.; Jermyn, M.; Gillams, A.; et al. Phase I/Ii Study of Verteporfin Photodynamic Therapy in Locally Advanced Pancreatic Cancer. *Br. J. Cancer* 2014, 110, 1698−1704.

(31) Banerjee, S. M.; El-Sheikh, S.; Malhotra, A.; Mosse, C. A.; Parker, S.; Williams, N. R.; MacRobert, A. J.; Hamoudi, R.; Bown, S. G.; Keshtgar, M. R. S. Photodynamic Therapy in Primary Breast Cancer. *J. Clin. Med.* 2020, 9, 483.

(32) Simões, J. C. S.; Sarpaki, S.; Papadimitroulas, P.; Therrien, B.; Loudos, G. Conjugated Photosensitizers for Imaging and Pdt in Cancer Research. *J. Med. Chem.* 2020, 63, 14119−14150.

(33) Miletto, I.; Gionco, C.; Paganini, M. C.; Cerrato, E.; Marchese, L.; Gianotti, E. Red Upconverter Nanocrystals Functionalized with Verteporfin for Photodynamic Therapy Triggered by Upconversion. *Int. J. Mol. Sci.* 2022, 23, 6951.

(34) Greco, A.; Garoffolo, G.; Chiesa, E.; Riva, F.; Dorati, R.; Modena, T.; Conti, B.; Pesce, M.; Genta, I. Nanotechnology, a Booster for the Multitarget Drug Verteporfin. *J. Drug Delivery Sci. Technol.* 2021, 64, 102562.

(35) Savellano, M. D.; Hasan, T. Photochemical Targeting of Epidermal Growth Factor Receptor: A Mechanistic Study. *Clin. Cancer Res.* 2005, 11, 1658−1668.

(36) Mahalingam, S. M.; Ordaz, J. D.; Low, P. S. Targeting of a Photosensitizer to the Mitochondrion Enhances the Potency of Photodynamic Therapy. *ACS Omega* 2018, 3, 6066−6074.

(37) Pellosi, D. S.; Paula, L. B.; de Melo, M. T.; et al. Targeted and Synergic Glioblastoma Treatment: Multifunctional Nanoparticles Delivering Verteporfin as Adjuvant Therapy for Temozolomide Chemotherapy. *Mol. Pharmaceut* 2019, 16, 1009−1024.

(38) Deng, W.; Kautzka, Z.; Chen, W. J.; et al. Plga Nanocomposites Loaded with Verteporfin and Gold Nanoparticles for Enhanced Photodynamic Therapy of Cancer Cells. *Rsc Adv.* 2016, 6, 112393−112402.

(39) Yang, M. S.; Jiang, D.; Chen, Z. L.; et al. Photodynamic Therapy of Drug-Resistant Human Colon Adenocarcinoma Using Verteporfin-Loaded Tpgs Nanoparticles with Tumor Homing and Penetrating Peptide Functionalization. *Rsc Adv.* 2016, 6, 100984−100992.

(40) Gu, X.; Shen, C.; Li, H.; Goldys, E. M.; Deng, W. X-Ray Induced Photodynamic Therapy (Pdt) with a Mitochondria-Targeted Liposome Delivery System. *J. Nanobiotechnol.* 2020, 18, 87.

(41) Brouwer, N. J.; Konstantinou, E. K.; Gragoudas, E. S.; et al. Targeting the Yap/Taz Pathway in Uveal and Conjunctival Melanoma with Verteporfin. *Invest Ophthalmol Vis Sci.* 2021, 62, 3.

(42) Ma, Y. W.; Liu, Y. Z.; Pan, J. X. Verteporfin Induces Apoptosis and Eliminates Cancer Stem-Like Cells in Uveal Melanoma in the Absence of Light Activation. *Am. J. Cancer Res.* **2016**, *6*, 2816−2830.

(43) Yu, F. X.; Luo, J.; Mo, J. S.; et al. Mutant Gq/11 Promote Uveal Melanoma Tumorigenesis by Activating Yap. *Cancer Cell* **2014**, *25*, 822−830.

(44) Wei, H.; Wang, F.; Wang, Y.; et al. Verteporfin Suppresses Cell Survival, Angiogenesis and Vasculogenic Mimicry of Pancreatic Ductal Adenocarcinoma Via Disrupting the Yap-Tead Complex. *Cancer Sci.* **2017**, *108*, 478−487.

(45) Barrette, A. M.; Ronk, H.; Joshi, T.; et al. Anti-Invasive Efficacy and Survival Benefit of the Yap-Tead Inhibitor Verteporfin in Preclinical Glioblastoma Models. *Neuro Oncol* **2022**, *24*, 694−707.

(46) Garcia-Rendueles, M. E. R.; Krishnamoorthy, G.; Saqcena, M.; Acuna-Ruiz, A.; Revilla, G.; de Stanchina, E.; Knauf, J. A.; Lester, R.; Xu, B.; Ghossein, R. A.; Fagin, J. A. Yap Governs a Lineage-Specific Neuregulin1 Pathway-Driven Adaptive Resistance to Raf Kinase Inhibitors. *Mol. Cancer* **2022**, *21*, 213.

(47) Brodowska, K.; Al-Moujahed, A.; Marmalidou, A.; et al. The Clinically Used Photosensitizer Verteporfin (Vp) Inhibits Yap-Tead and Human Retinoblastoma Cell Growth in Vitro without Light Activation. *Exp. Eye Res.* **2014**, *124*, 67−73.

(48) Wang, C.; Zhu, X. Y.; Feng, W. W.; Yu, Y.; Jeong, K.; Guo, W.; Lu, Y.; Mills, G. B. Verteporfin Inhibits Yap Function through up-Regulating 14−3-3 Sigma Sequestering Yap in the Cytoplasm. *Am. J. Cancer Res.* **2016**, *6*, 27−37.

(49) Pobbati, A. V.; Hong, W. A Combat with the Yap/Taz-Tead Oncoproteins for Cancer Therapy. *Theranostics* **2020**, *10*, 3622−3635.

(50) Donohue, E.; Thomas, A.; Maurer, N.; et al. The Autophagy Inhibitor Verteporfin Moderately Enhances the Antitumor Activity of Gemcitabine in a Pancreatic Ductal Adenocarcinoma Model. *J. Cancer* **2013**, *4*, 585−596.

(51) Song, S.; Ajani, J. A.; Honjo, S.; et al. Hippo Coactivator Yap1 Upregulates Sox9 and Endows Esophageal Cancer Cells with Stem-Like Properties. *Cancer Res.* **2014**, *74*, 4170−4182.

(52) Yu, F. X.; Luo, J.; Mo, J. S.; et al. Mutant Gq/11 Promote Uveal Melanoma Tumorigenesis by Activating Yap. *Cancer Cell* **2014**, *25*, 822−830.

(53) Jiu, X. D.; Liu, Y.; Wen, J. Artesunate Combined with Verteporfin Inhibits Uveal Melanoma by Regulation of the Malat1/Yes-Associated Protein Signaling Pathway. *Oncol. Lett.* **2021**, *22*, 597.

(54) Li, M.; Sun, J.; Zhang, W.; et al. Drug Delivery Systems Based on Cd44-Targeted Glycosaminoglycans for Cancer Therapy. *Carbohydr. Polym.* **2021**, *251*, No. 117103.

(55) Sun, Y. Y.; Keller, K. E. Hyaluronan Cable Formation by Ocular Trabecular Meshwork Cells. *Exp. Eye Res.* **2015**, *139*, 97−107.

(56) Mandal, A.; Bisht, R.; Rupenthal, I. D.; et al. Polymeric Micelles for Ocular Drug Delivery: From Structural Frameworks to Recent Preclinical Studies. *J. Controlled Release* **2017**, *248*, 96−116.

(57) Bai, Y.; Liu, C. P.; Chen, D.; et al. Beta-Cyclodextrin-Modified Hyaluronic Acid-Based Supramolecular Self-Assemblies for Ph- and Esterase- Dual-Responsive Drug Delivery. *Carbohydr. Polym.* **2020**, *246*, No. 116654.

(58) Trujillo-de Santiago, G.; Sharifi, R.; Yue, K.; et al. Ocular Adhesives: Design, Chemistry, Crosslinking Mechanisms, and Applications. *Biomaterials* **2019**, *197*, 345−367.

(59) Chai, Z.; Teng, C.; Yang, L.; et al. Doxorubicin Delivered by Redox-Responsive Hyaluronic Acid-Ibuprofen Prodrug Micelles for Treatment of Metastatic Breast Cancer. *Carbohydr. Polym.* **2020**, *245*, No. 116527.

(60) Zhang, L. W.; Gao, S.; Zhang, F.; et al. Activatable Hyaluronic Acid Nanoparticle as a Theranostic Agent for Optical/Photoacoustic Image-Guided Photothermal Therapy. *ACS Nano* **2014**, *8*, 12250−12258.

(61) Wang, G. H.; Gao, S.; Tian, R.; et al. Theranostic Hyaluronic Acid-Iron Micellar Nanoparticles for Magnetic-Field-Enhanced Invivo Cancer Chemotherapy. *Chemmedchem* **2018**, *13*, 78−86.

(62) Zhu, L.; Zhao, Y.; Liu, T.; et al. Inhibition of Nadph Oxidase-Ros Signal Using Hyaluronic Acid Nanoparticles for Overcoming Radioresistance in Cancer Therapy. *ACS Nano* **2022**, *16*, 18708−18728.

(63) Danen, E. H.; ten Berge, P. J.; van Muijen, G. N.; et al. Expression of Cd44 and the Pattern of Cd44 Alternative Splicing in Uveal Melanoma. *Melanoma Res.* **1996**, *6*, 31−35.

(64) Salwowska, N. M.; Bebenek, K. A.; Zadlo, D. A.; et al. Physiochemical Properties and Application of Hyaluronic Acid: A Systematic Review. *J. Cosmet Dermatol* **2016**, *15*, 520−526.

(65) Kadu, P. J.; Kushare, S. S.; Thacker, D. D.; et al. Enhancement of Oral Bioavailability of Atorvastatin Calcium by Self-Emulsifying Drug Delivery Systems (Sedds). *Pharm. Dev Technol.* **2011**, *16*, 65−74.

(66) Chen, C.; Zhao, S.; Karnad, A.; Freeman, J. W. The Biology and Role of Cd44 in Cancer Progression: Therapeutic Implications. *J. Hematol. Oncol.* **2018**, *11*, 64.

(67) Platt, V. M.; Szoka, F. C., Jr. Anticancer Therapeutics: Targeting Macromolecules and Nanocarriers to Hyaluronan or Cd44, a Hyaluronan Receptor. *Mol. Pharmaceutics* **2008**, *5*, 474−486.

(68) Bouga, H.; Tsouros, I.; Bounias, D.; Kyriakopoulou, D.; Stavropoulos, M. S; Papageorgakopoulou, N.; Theocharis, D. A; Vynios, D. H Involvement of Hyaluronidases in Colorectal Cancer. *BMC Cancer* **2010**, *10*, 499.

(69) Krupkova, O.; Greutert, H.; Boos, N.; et al. Expression and Activity of Hyaluronidases Hyal-1, Hyal-2 and Hyal-3 in the Human Intervertebral Disc. *Eur. Spine J.* **2020**, *29*, 605−615.

(70) Li, P.; He, K.; Li, J.; et al. The Role of Kupffer Cells in Hepatic Diseases. *Mol. Immunol* **2017**, *85*, 222−229.

(71) Daňková, J.; Buzgo, M.; Vejpravová, J.; et al. Highly Efficient Mesenchymal Stem Cell Proliferation on Poly-E-Caprolactone Nanofibers with Embedded Magnetic Nanoparticles. *Int. J. Nanomedicine* **2015**, *10*, 7307−7317.

(72) Yang, G.; Ni, J. S.; Li, Y.; et al. Acceptor Engineering for Optimized Ros Generation Facilitates Reprogramming Macrophages to M1 Phenotype in Photodynamic Immunotherapy. *Angew. Chem., Int. Ed. Engl.* **2021**, *60*, 5386−5393.

(73) Tan, L.; Shen, X.; He, Z.; et al. The Role of Photodynamic Therapy in Triggering Cell Death and Facilitating Antitumor Immunology. *Front Oncol* **2022**, *12*, No. 863107.

(74) Stampouloglou, E.; Cheng, N.; Federico, A.; et al. Yap Suppresses T-Cell Function and Infiltration in the Tumor Microenvironment. *PLoS Biol.* **2020**, *18*, No. e3000591.